ADVANCES IN ATMOSPHERIC SCIENCES, VOL. 40, MAY 2023, 874–886

• **Original Paper** •

Microphysical Characteristics of Extreme-Rainfall Convection over the Pearl River Delta Region, South China from Polarimetric Radar Data during the Pre-summer Rainy Season※

Hao HUANG[1,2], Kun ZHAO[*1,2], Johnny C. L. CHAN[3], and Dongming HU[4]

[1]*Key Laboratory for Mesoscale Severe Weather/MOE and School of Atmospheric Sciences, Nanjing University, Nanjing* 210023, *China*

[2]*State Key Laboratory of Severe Weather and Joint Center for Atmospheric Radar Research, CMA/NJU, Beijing* 100081, *China*

[3]*School of Energy and Environment, City University of Hong Kong, Hong Kong* 999077, *China*

[4]*Guangdong Meteorological Observatory, Guangzhou* 510062, *China*

(Received 13 August 2021; revised 14 January 2022; accepted 9 February 2022)

ABSTRACT

During the pre-summer rainy season, heavy rainfall occurs frequently in South China. Based on polarimetric radar observations, the microphysical characteristics and processes of convective features associated with extreme rainfall rates (ERCFs) are examined. In the regions with high ERCF occurrence frequency, sub-regional differences are found in the lightning flash rate (LFR) distributions. In the region with higher LFRs, the ERCFs have larger volumes of high reflectivity factor above the freezing level, corresponding to more active riming processes. In addition, these ERCFs are more organized and display larger spatial coverage, which may be related to the stronger low-level wind shear and higher terrain in the region. In the region with lower LFRs, the ERCFs have lower echo tops and lower-echo centroids. However, no clear differences of the most unstable convective available potential energy (MUCAPE) exist in the ERCFs in the regions with different LFR characteristics. Regardless of the LFRs, raindrop collisional coalescence is the main process for the growth of raindrops in the ERCFs. In the ERCFs within the region with lower LFRs, the main mechanism for the rapid increase of liquid water content with decreasing altitude below 4 km is through the warm-rain processes converting cloud drops to raindrops. However, in those with higher LFRs, the liquid water content generally decreases with decreasing altitude.

Key words: microphysics, extreme rainfall rate, polarimetric radar, lightning flash rate

Citation: Huang, H., K. Zhao, J. C. L. Chan, and D. M. Hu, 2023: Microphysical characteristics of extreme-rainfall convection over the Pearl River Delta region, South China from polarimetric radar data during the pre-summer rainy season. *Adv. Atmos. Sci.*, **40**(5), 874–886, https://doi.org/10.1007/s00376-022-1319-8.

Article Highlights:

- Clear differences in microphysics of the extreme-rainfall convective features found in regions with different lighting flash rates.
- Stronger low-level wind shear and higher terrain may favor the organization and ice processes of the extreme-rainfall convection.

1. Introduction

As an important component of the East Asian monsoon, the South China Sea (SCS) monsoon has a large impact on the life of massive populations (Ding et al., 2004). Under its influence, south China experiences heavy rainfall every year. Some extreme rainfall cases can cause flooding and landslide hazards. This makes accurate rainfall prediction critically important for human society and natural systems (Piao et al., 2010). In numerical models, the accuracy of rainfall estimation is closely related to the uncertainties in the microphysical parameterization (Sun, 2005; Li et al., 2012). Because of the influence of the SCS monsoon, the environmental conditions in south China (e.g., abundant low-level moisture) are gener-

※ This paper is a contribution to the special issue on the 14th International Conference on Mesoscale Convective Systems and High-Impact Weather.

* Corresponding author: Kun ZHAO
Email: zhaokun@nju.edu.cn

ally different from that over other continental regions (Xu et al., 2009). This might lead to unique microphysical structures and processes in south China (e.g., general increasing reflectivity factor towards the ground) (Liu and Zipser, 2013b). A better understanding of the microphysics in extreme rainfall in south China could help improve its prediction.

Using ground-based and space-borne radars, the microphysics of heavy rainfall has been investigated in many parts of the world (Liu and Zipser, 2009; Hamada et al., 2015; Dolan et al., 2018; Chen et al., 2019a, b; Nielsen and Schumacher, 2020). In these studies, two different mechanisms are proposed for heavy rain formation: one is mainly characterized by active warm-rain growth processes (auto-conversion and accretion) and the other is mainly characterized by ice-based growth processes (mainly riming) (Petersen and Rutledge, 1998; Vitale and Ryan, 2013; Hamada et al., 2015). These different microphysical mechanisms can also lead to different macro- and microphysical characteristics of the precipitating systems. The warm-rain processes usually have high precipitation efficiency, and the corresponding systems tend to have lower echo tops and lower-echo centroids than those dominated by ice-based processes (Vincent et al., 2003; Liu et al., 2012). In addition, the raindrop size distributions (DSDs) produced by warm-rain processes tend to consist of a high number concentration of small-sized drops; in comparison, when ice-based growth is the dominant process, the DSDs skew towards a low number concentration of large-sized drops (Bringi et al., 2003; Vitale and Ryan, 2013).

Lightning is another important indicator of microphysical processes. As revealed in many studies (Goodman et al., 1988; Saunders, 1993; e.g., Carey and Rutledge, 2000; Vincent et al., 2003; Gauthier et al., 2006; Deierling et al., 2008), in the precipitating systems dominated by ice-based growth, the collision between riming graupel particles and smaller ice particles in the presence of supercooled water would facilitate the thunderstorm charging processes (Saunders, 1993). However, lightning processes are not necessarily associated with precipitating systems dominated by warm-rain processes (Petersen and Rutledge, 1998; Hamada et al., 2015).

Environmental conditions are crucial for microphysical processes. A deep and wet warm cloud layer is usually required for the dominance of warm-rain processes (Petersen and Rutledge, 1998; Hamada et al., 2015). However, if the ice-based growth (e.g., riming) is dominant for rainfall formation, a more unstable environment and an increased updraft strength are required (Hamada et al., 2015; Takahashi et al., 2015). Regions under the influence of monsoon (e.g., South China) usually have complex environmental conditions, which could lead to a combination of two different mechanisms for heavy rain there (Xu and Zipser, 2012). The underlying surface (e.g., topography and urban areas) in south China also adds to the complexity of microphysics for extreme rainfall and the associated mechanisms.

In recent years, a number of polarimetric weather radars and a lightning detection network have been established in south China. These data can provide important information to address the dominant microphysical characteristics for extreme rainfall in south China and the associated weather conditions, which is the motivation for this study. The rest of this paper is organized as follows. Detailed procedures for the processing of radar data and lightning data are described in section 2. Analyses of the microphysical structures and processes are presented in section 3. Conclusions and discussions are given in section 4.

2. Data and Methodology

The study is mainly based on the observations taken from an S-band polarimetric radar located at Guangzhou City in the Pearl River Delta region, south China (named Guangzhou S-POL) in May and June from 2016 to 2018. Guangzhou S-POL is a part of the weather surveillance radar network in China and has a 6-minute sampling time interval for its full volumetric scans. The other parameters of the radar and the data quality procedures (including the bias correction of differential reflectivity Z_{DR}, removal of non-meteorological echoes, process of total differential phase Ψ_{DP}) can be found in Huang et al. (2018). In particular, the specific differential phase K_{DP} used in this study is calculated using the least square fitting algorithm to keep consistency between the observations of liquid and non-liquid hydrometeors (Istok et al., 2009).

The radar volume scans were interpolated onto a 3-dimensional Cartesian grid with 1.0-km horizontal and 0.5-km vertical grid spacing using the Radx C++ library developed by the National Center for Atmospheric (Dixon, 2015). Then, the horizontal reflectivity factor Z_H at an altitude of 3 km was used to classify the precipitation into two types: convective and stratiform by adopting the method proposed by Steiner et al. (1995). Similar to Liu and Zipser (2013a), the convective features (CFs) are identified by the contiguous grid points of convective regions. Note that only the data within 125 km distance from the radar site are used in this study considering the uncertainty caused by radar beam broadening. One example of the gridded radar scan at 3 km in altitude observed by Guangzhou S-POL at 0930 UTC 15 May 2016 is shown in Fig. 1a. A convective line with trailing stratiform echoes is observed by the radar. The maximum Z_H exceeds 55 dBZ. The identified CFs show large differences in intensity, areas, and structure, which are related to differences in the dynamical and microphysical processes.

Since the spatial distribution of rain gauges in south China is non-uniform, polarimetric quantitative precipitation estimation (QPE) products were used to obtain the mean rainfall rate (R) for each CF. For the QPE products, a composite strategy was applied to the plan position indicator (PPI) radar scans. First, the hydrometeor identification (HID) algorithm adapted for S-band (Dolan et al., 2013) was used to classify the precipitation into 10 classes. For three liquid classes (drizzle, rain, and big drops), a composite rainfall estimator

was applied (Bringi et al., 2011), with the relationships adapted as in Huang et al. (2020). To clarify, three polarimetric rainfall estimators $R(Z_H)$, $R(Z_H, Z_{DR})$, and $R(K_{DP})$ were composited based on the values of Z_H, Z_{DR}, and K_{DP}. For the radar gates classified as non-liquid classes, the method stated in Chen et al. (2017) was used. Then, the rainfall rate estimates at the PPI scans were bilinearly interpolated to the 2-dimensional horizontal Cartesian grid corresponding to the 3-D grid above. Within a 75 km distance from the radar site, the rainfall rate estimates at the 1.5-degree elevation were used in the interpolation; otherwise, those at the 0.5-degree elevation were used, which helped to mitigate ground clutter contamination. Afterwards, we calculated a mean rainfall rate for each CF by averaging the estimates at the corresponding grid points.

For the microphysics study, the liquid water content (LWC) and ice water content (IWC) were estimated for the gridded data using the method in Cifelli et al. (2002), but with the parameterization relationships between LWC and the radar variables (Z_H and Z_{DR}) optimized using local DSD observations (not shown). The DSDs were retrieved from Z_H and Z_{DR} at the grid points classified as liquid hydrometeors by the HID algorithm assuming a constrained-gamma DSD model (Zhang et al., 2001), with the shape-slope relationship adapted for south China (Huang et al., 2020). The mass-weighted mean diameters D_m (mm), and generalized intercept parameter N_w (mm^{-1} m^{-3}) were calculated from the retrieved DSDs for analysis.

To supply more information, we also matched the rate of lightning flashes observed by an EarthNetworks Total Lightning System (ENTLS) (Naccarato et al., 2013) deployed by Guangdong Province to the horizontal plane of the radar grid, with both intra-cloud and cloud-to-ground discharges included. For each radar grid point, the number of lightning flashes that occurred within the grid over the 6-minute interval starting from the beginning of the radar volume scan was counted. The lightning flash rate (LFR) for the grid is defined as the lightning flash number normalized by the grid area of 1 km^2 and the time interval of 6 minutes, which has a unit of km^{-2} h^{-1}. As shown in the matched LFRs in Fig. 1a, part of the frontal convective line is associated with LFR greater than 20 km^{-2} h^{-1}; however, the value of LFR is not simply correlated to the value of Z_H. Furthermore, since lightning flash rates may be positively correlated to echo top heights (Vincent et al., 2003; Liu et al., 2012), the 35-dBZ echo tops were also calculated for each column of the 3-D grid for verification, by vertically interpolating between grid points that bracket the echo-top threshold (35 dBZ here).

3. Results

3.1. *Definition and distribution of CFs with extreme rainfall rate*

The probability density function for the mean rainfall rates of the CFs within the 125-km range from the radar site is shown in Fig. 1b. In May–June 2016–18, more than 260 000 CFs were detected by Guangzhou S-POL. Most of the CFs have a mean rainfall rate lower than 10 mm h^{-1}. The maximum value of the probability density function of the CF-mean rainfall rates occurs at ~3.5 mm h^{-1}. When the

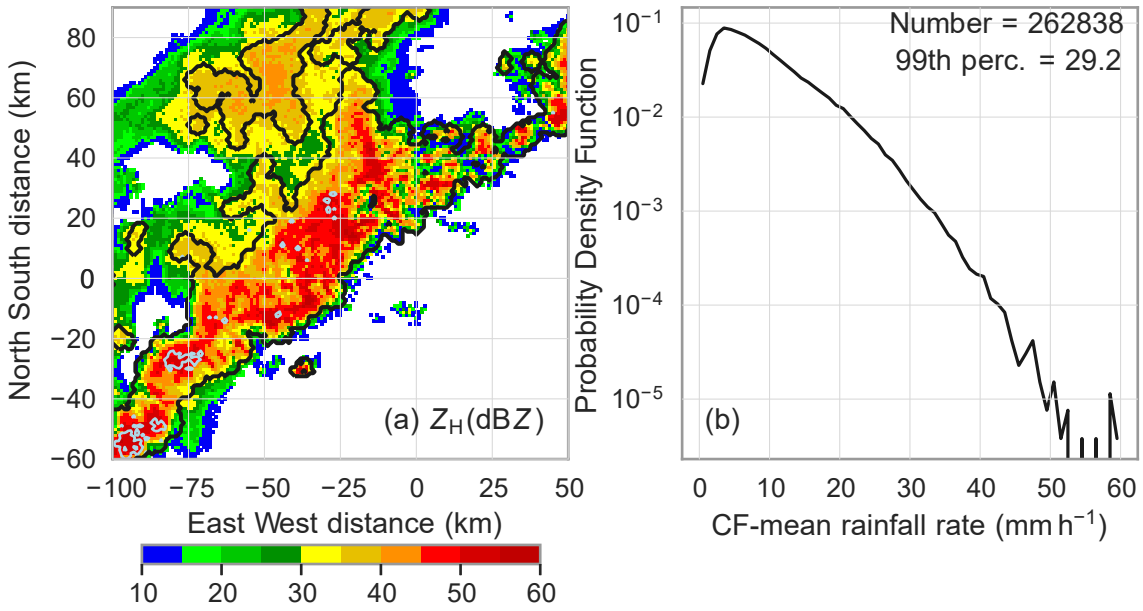

Fig. 1. (a) Schematic of one gridded radar scan (Z_H) at 3 km in altitude containing several CFs observed by Guangzhou S-POL at 0930 UTC 15 May 2016. Each CF identified by contiguous convective regions is shown by a black contour. The light blue contours represent the regions with lightning flash rates higher than 20 km^{-2} h^{-1}. The origin is the location of Guangzhou S-POL. (b) The probability density function for the mean rainfall rates of the CFs within 125 km from the radar site.

CF-mean rainfall rate is greater than 3.5 mm h^{-1}, the frequency of CF generally decreases exponentially. The 99th percentile of the distribution is 29.2 mm h^{-1}. Accordingly, the CFs with a mean rainfall rate greater than 29.2 mm h^{-1} are defined as CFs with extreme rainfall rates or extreme-rainfall-rate CFs (ERCFs), with the total number exceeding 2600.

The distribution of occurrence frequency of the ERCFs is shown in Fig. 2a. It is found that there are two clear occurrence centers. The first is about 100 km to the south of the radar (near the coastline), which is out of the optimal observation range of the radar and will not be further studied in this study. Another occurrence center extends from 20 km south of the radar site to most regions to the north and northwest. Figure 2b exhibits the distribution of the mean LFR in the same domain, which shows large non-uniformity. It is found that large mean LFR values exist to the north and northwest of the domain (50 to 100 km in the north-south direction), but LFR values are generally lower in the other regions, especially to the northeast of the radar site (0–40 km in the east-west direction and 0–50 km in the north-south direction). As the lightning rate is an indicator of the graupel-ice collision process, the non-uniformity of LFRs may imply different roles of ice microphysics in the formation of extreme rain in the ERCFs.

3.2. *Microphysical characteristics and processes of the ERCFs*

To further investigate how the LFR is related to the microphysics of the ERCFs, two sub-regions of interest (Fig. 2a) are subjectively selected, mainly based on the distributions of the LFRs and the surface conditions. As indicated by the adjacent black rectangles in Fig. 2, region A is characterized by higher terrains. On the other hand, region B is nearer the radar site. Most of the underlying surface of region B is urban according to the DMSP/OLS (Defense Meteorological Satellite Program/Operational Linescan System) nighttime light data. The ERCFs have a higher mean LFR in region A and a relatively lower value in region B (Fig. 2b).

Figure 3 exhibits some properties of the ERCFs in regions A and B. Note that to determine whether a CF belongs to the two regions (A or B), a Z_H-normalized center $(\bar{x}, \bar{y})$ is calculated for the CF, following $\bar{x} = \sum_{i=1}^{n}\left(x_i Z_h^i\right)/\sum_{i=1}^{n} Z_h^i$ and $\bar{y} = \sum_{i=1}^{n}\left(y_i Z_h^i\right)/\sum_{i=1}^{n} Z_h^i$, where Z_h^i (in $mm^6\ m^{-3}$) is the linear value of Z_H ($Z_h = 10^{0.1Z_H}$) at 3 km in altitude for the grid point (x_i, y_i), and n is the total number of grid points of the CF. To evaluate the differences in the ERCF properties in regions A and B, the Mann-Whitney U test is used (McKnight and Najab, 2010). In Fig. 3a, it is found that the distributions of the mean LFR in both two regions are positively skewed. A wider distribution of the mean LFR exists in region A with a significantly higher (p-value < 0.01) median value (see also Fig. 2b), indicative of stronger storm updrafts (Deierling et al., 2008). In Fig. 3b, the mean and median values of the CF-mean 35-dBZ echo tops are also significantly larger (p-value < 0.01) in region

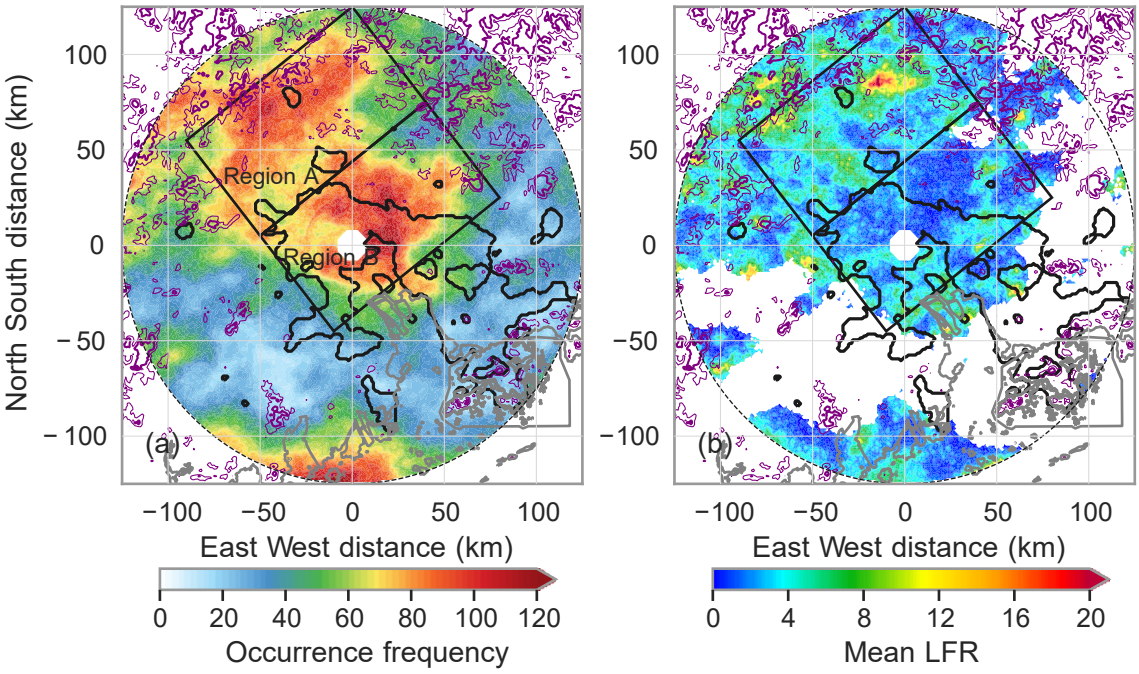

Fig. 2. (a) Distribution of occurrence frequency of the echoes in the ERCFs (more than 2600) in May–June 2016–18. Two rectangles represent the regions of interest: Region A and Region B. (b) Distribution of mean lightning flash rate of the ERCFs in (a) at each grid. The regions with occurrence frequency of the ERCFs in (a) lower than 40 are masked. The origin is the location of Guangzhou S-POL. The grey curves represent coastlines. The purple contours represent the topography (the thinner for 250 m and the thicker for 500 m). The black contours represent the regions where DMSP/OLS nighttime light data is greater than 56.

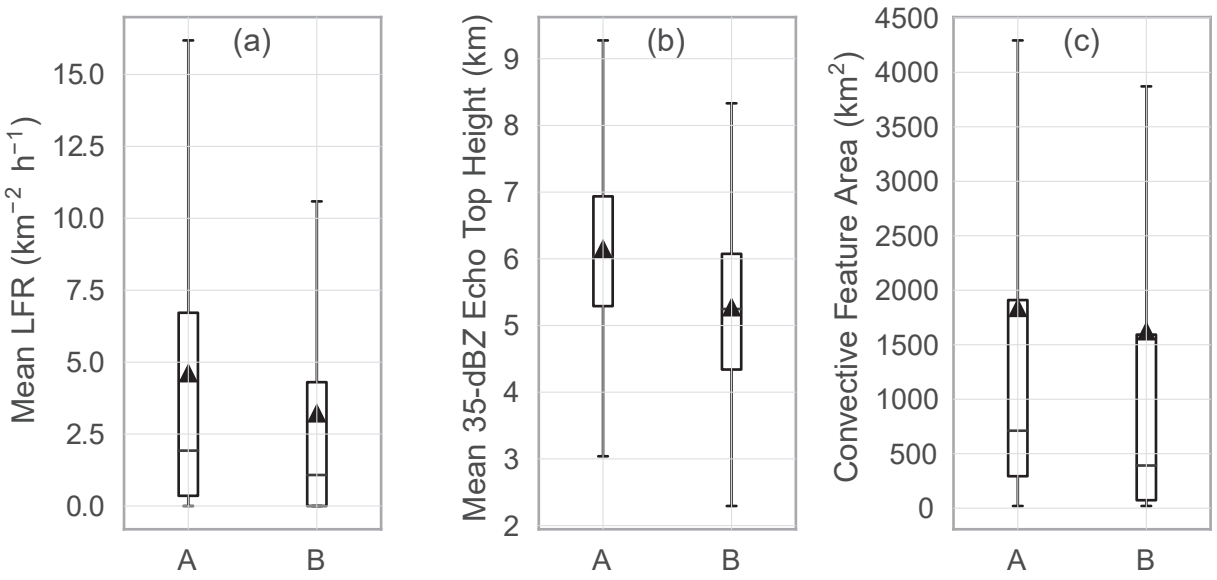

Fig. 3. Box plots for (a) the CF-mean lightning flash rates, (b) 35-dB*Z* echo top heights, and (c) the ERCFs' areas at the altitude of 3 km corresponding to the ERCFs whose reflectivity factor-normalized center is located in region A or region B (*x*-axis). The upper and lower edges of the boxes represent the quartile values, and the line in the box (triangle) is the median (mean). The range of the data is shown by the whiskers extending from the box.

A than those in region B. This may be another indicator of stronger updrafts in region A (Doswell III, 1985; Xu and Zipser, 2012). As pointed out in previous studies (Goodman et al., 1988; Carey and Rutledge, 2000; Vincent et al., 2003; Deierling et al., 2008), stronger updrafts can facilitate the transport of supercooled liquid water to the layers above the freezing level and the riming process essential for graupel growth and lightning in region A (Fig. 2b), Finally, the areas of the ERCFs at the altitude of 3 km are checked in Fig. 3c. The distributions of CF areas are positively skewed in both regions A and B, i.e., only a small part of the CFs have large areas. The mean and median values of the areas are relatively greater in region A than those in region B. As a result, the ERCFs with much higher echo tops (in region A) would probably have larger volumes with reflectivity values greater than 35-dB*Z* above the freezing level than those in region B. The result also proves the positive correlation between the volumes and LFRs, as documented in Vincent et al. (2003) and Liu et al. (2012).

To further illustrate the associated microphysical properties in the two regions, Fig. 4 shows the spatial distributions of the retrieved mean IWC at an altitude of 5.5 km (right above the melting level) and the mean LWC, D_m, and N_w at the altitude of 3 km (below the melting level) of the ERCFs. Note that in May and June, the freezing level (0°C) is about 5 km over the Pearl River Delta. In Fig. 4a, it is found that the mean IWC values of the ERCFs at the 5.5-km altitude are clearly greater in region A. The greater ice-phased hydrometeor existence in region A is also evidence for a more active ice (riming) process, which causes more lightning (a higher mean LFR in Fig. 2b) (Carey and Rutledge, 2000; Deierling et al., 2008). The mean LWC values of the ERCFs at the 3-km altitude (Fig. 4b) are also larger in region A but smaller in region B, probably due to the melting of the hydrometeors with greater IWCs in region A. Besides, the microphysical processes below the melting level would also contribute to the LWCs, which will be studied further later. Comparing the distributions of the mean D_m at the 3-km altitude (Fig. 4c) in the two selected regions of interest, it is found that the D_m in region B is less uniform and shows a low-value center (near the radar site). The generally larger D_m values in region A, indicating the larger mean raindrops in the ERCFs, would be attributed to the melting of more or larger graupel particles there, which is consistent with previous studies (e.g., Cifelli et al., 2002; Bringi et al., 2003). Besides, the mean N_w values at the 3-km altitude are also slightly larger in region A (Fig. 4d), which are consistent with those of LWC and D_m.

Figure 5 shows the mean of the ERCF vertical profiles of polarimetric radar variables (Z_H, Z_{DR}, and K_{DP}) and the derived microphysical variables (LWC, IWC, and D_m). In the mean vertical profiles of Z_H (Fig. 5a) and Z_{DR} (Fig. 5b), no significant bright band is found. Above the freezing level, the mean Z_H (Z_{DR}) is generally higher (lower) in region A (solid lines), also suggesting the existence of larger or more graupel particles. The lower Z_H and larger Z_{DR} values in region B indicate the presence of relatively more ice crystals and aggregates, corresponding to the larger K_{DP} (Fig. 5b). The increases of Z_H with decreasing altitude above the melting layer mainly denote the riming and aggregation processes, as well as the updraft's capability to lift the supercooled liquid drops and water vapor to the layers above the freezing level being weakened with increasing altitude (Fig. 5).

Below the melting layer, the Z_H is higher in region A than in region B above the 2-km altitude and gets slightly lower below 2 km. Meanwhile, the Z_{DR} values below 5 km

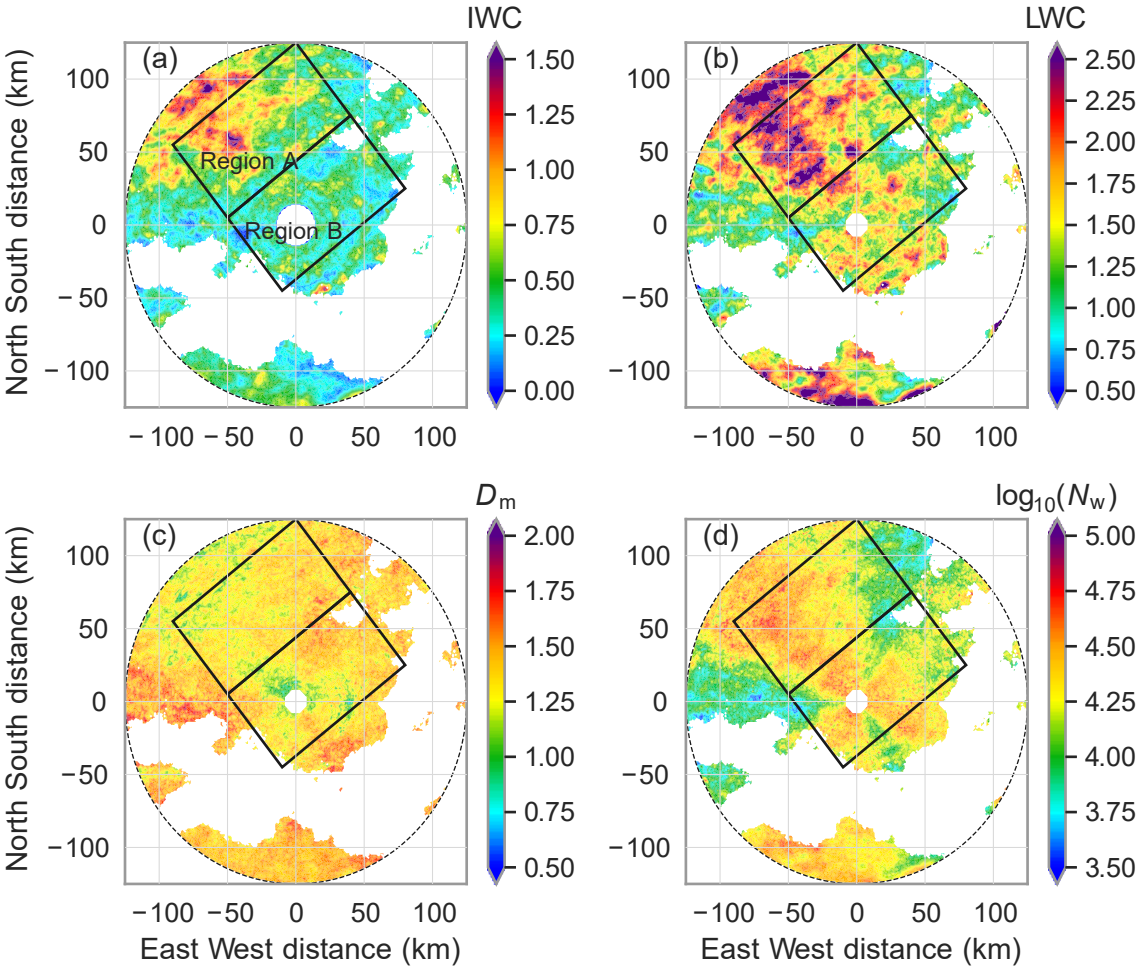

Fig. 4. Distributions of the mean (a) IWC at the 5.5-km altitude, (b) LWC at the 3-km altitude, (c) D_m at the 3-km altitude, and (d) N_w at 3-km altitude retrieved from the radar measurements of the ERCFs (more than 2600) in May-June 2016–18. Two rectangles represent regions A and B, respectively. The regions with occurrence frequency lower than 40 are masked. The origin is the location of Guangzhou S-POL.

are greater in region A, indicating larger mean raindrop sizes there. This is consistent with the mean D_m from the retrieved DSD (Fig. 5d). In addition, the larger Z_H and Z_{DR} in region A below the melting layer are mainly attributed to the melting of larger or more graupel particles as well as the more active auto-conversion and accretion processes converting cloud water to rainwater (Wu et al., 2018). This also results in the larger mean K_{DP} in region A (Fig. 5b). Besides, the mean Z_H and Z_{DR} (as well as D_m) increases with decreasing altitude below the freezing level in both regions A and B are probably due to raindrop collision and coalescence (Kumjian and Prat, 2014), which will be further discussed in Fig. 6. Note that the raindrop collision and coalescence mentioned here is the process between raindrops only without the inclusion of cloud drops, which would not lead to the change in water content.

In Fig. 5c, the IWC profiles in region A are generally higher, corresponding to the larger Z_H (Fig. 5a) there. The peak values of the IWCs are at about 5.5 km in altitude. Above this altitude, the IWCs increase with decreasing altitude due to the aggregation and riming processes. Below this altitude, the IWCs generally decrease with decreasing altitude because of the melting process. The mean LWC profiles are also generally higher in region A than in region B (above 2 km in altitude). In region B, the ratio of the peak IWC value (0.430 g m^{-3}) to the LWC at 4 km in altitude (1.41 g m^{-3}), where the mean IWC is close to 0 g m^{-3}, is about 0.30. However, in region A, the ratio of the peak IWC value (0.603 g m^{-3}) to the 4-km-altitude LWC (1.74 g m^{-3}) is about 0.35. This generally means that the melting of ice hydrometeors generated by ice microphysical processes plays a more important role in the rainfall of the ERCFs in region A than in region B.

In Fig. 5c, it is also found that the changes of the mean LWC profiles in terms of height are different between regions A and B. To further study the relevant microphysical processes below the melting layer, the mean Z_{DR} changes (ΔZ_{DR}) as a function of the mean LWC changes (ΔLWC) over the layers between 1–3 km (squares), 3–4 km (dots), and 3–5 km (triangles) for ERCFs in the two regions is given in Fig. 6, in which the mean Z_H changes (ΔZ_H) are shown by the color of the symbols. The ΔLWC values over

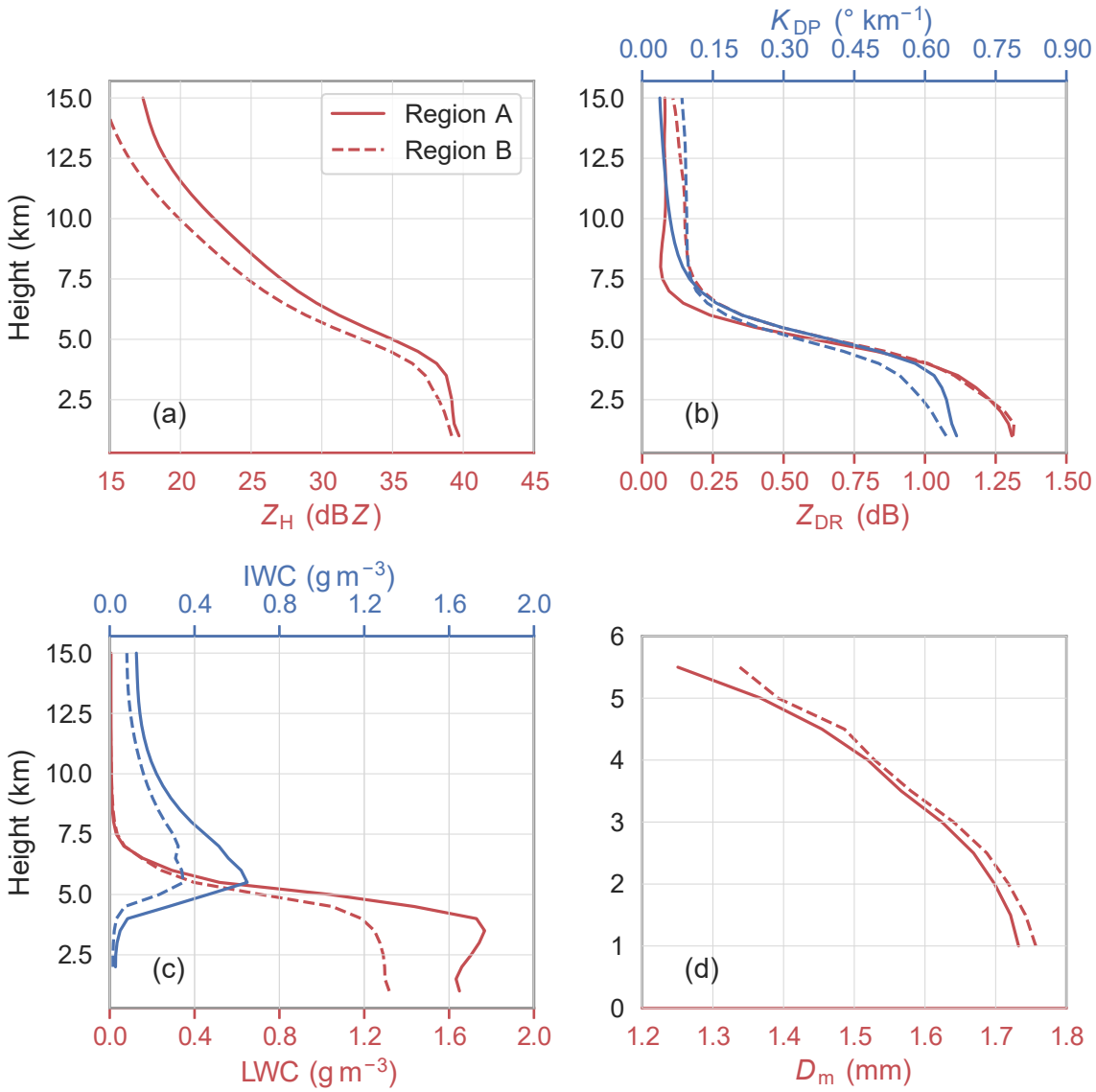

Fig. 5. Mean ERCF vertical profiles with reflectivity factor-normalized centers located in region A (solid lines) and region B (dashed lines) corresponding to (a) Z_H (red), (b) Z_{DR} (red), K_{DP} (blue), (c) LWC (red), IWC (blue), and (d) D_m (red).

the three layers in the two regions show clear differences. Over the 4–5 km layer, the ΔLWC values in both region A and region B are positive and have the largest magnitudes within the three layers. This mainly indicates that the growth of the water content in the ERCFs is contributed from the melting process and the warm-rain processes (autoconversion and accretion) (Wu et al., 2018). Over the layers between 3–4 km and between 1–3 km, a difference can be found in the ΔLWC values between the two regions. The positive ΔLWC values (increases in the LWCs with decreasing altitude) in region B suggest the importance of warm-rain growth processes for the ERCFs. However, in region A, the negative ΔLWC values are possibly due to the evaporation process probably in the downdrafts or incomplete melting of ice particles (Kumjian and Ryzhkov, 2010; Liu and Zipser, 2013b; Wang et al., 2018). Despite the differences in the microphysical processes below the 4-km altitude, the mean LWC values of the ERCFs at 1 km in altitude in regions A and B are similar (red lines in Fig. 5c). In addition, the ΔZ_H and ΔZ_{DR} for all the selected layers are positive in both regions A and B. This is probably due to the raindrop collision and coalescence process (Kumjian and Prat, 2014), resulting in the downward growth of the mean raindrop sizes in both regions.

3.3. *Environmental analysis for regional CF differences*

The reasons for the different microphysical characteristics and processes of ERCFs in regions A and B are analyzed in this section. Considering the difficulty in the retrieval of wind field matching with the microphysical field, the hourly ERA5 reanalysis dataset (0.25°) (Hersbach et al., 2020) is used. Following Hamada et al. (2015), Vitale and Ryan (2013), and Takahashi et al. (2015), we calculated the most

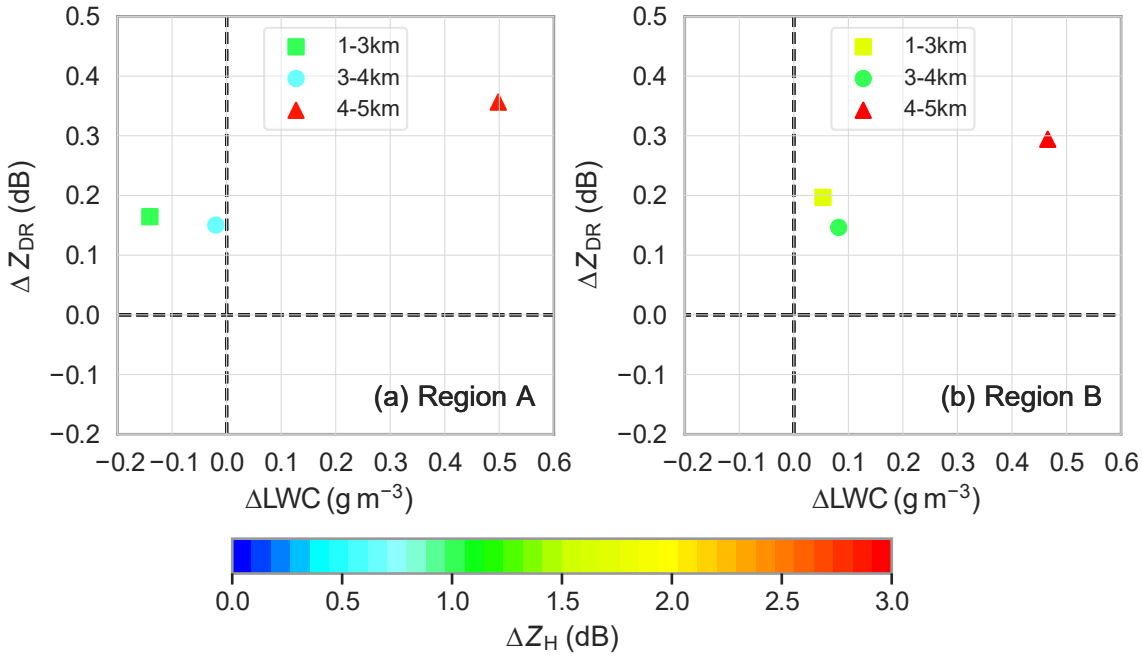

Fig. 6. The vertical change in the mean Z_{DR} (ΔZ_{DR}) as a function of the change in the mean LWC (ΔLWC) over the layers between 1 and 3 km in altitude (squares), between 3 and 4 km in altitude (circles), and between 4 and 5 km in altitude (triangles) in the ERCFs in region A (a) and region B (b). The color of the symbols represents the change in the mean Z_H (ΔZ_H) in the same layer. ΔZ_H, ΔZ_{DR}, and ΔLWC are the corresponding values at the bottom of the layer minus those at the top of the layer.

unstable convective available potential energy (MUCAPE), warm cloud depth (WCD) between the lifted condensation level (LCL) to the –10°C level (Brauer et al., 2020), the precipitable water (PW) in the warm cloud layer, relative humidity at 700 hPa, and the low-level wind shear between the LCL and 700-hPa level for the ERCFs using the ERA5 dataset, as shown in Fig. 7. In the calculation, the profiles closest to the Z_H-normalized center of the ERCFs are extracted from the ERA5 reanalysis dataset and input into the MetPy package (May and Bruick, 2019). The distributions of terrain heights over the radar grids in regions A and B are also shown in Fig. 7f.

In Fig. 7a, the distributions of the MUCAPE for the CFs in the two regions only show a slight difference in their widths and no clear differences in the mean and median values (>2000 J kg^{-1}). This mainly implies a dynamical mechanism different from those in Hamada et al. (2015) and Takahashi et al. (2015), which will be further discussed later. In Fig. 7b, the ERCFs have a wider distribution of WCDs in region A. Deep mean WCDs are found for ERCFs in both regions (> 6500 m), which is only slightly larger in region B. In Figs. 7c–d, we can find relatively larger mean (and median) values of PW and relative humidity at 700 hPa for the ERCFs in region B, in which the differences are significant according to the *p*-values of the Mann-Whitney U test (0.017 and 0.0002, respectively). This generally indicates more water vapor below the melting layer in region B than in region A, which corresponds to its more dominant warm-rain processes (converting cloud drops to raindrops).

In Fig. 7e, a significantly stronger mean low-level wind shear is found in region A, which is probably one of the main reasons leading to the more organized systems with larger areas (in Fig. 3c) (Chen et al., 2015). For verification, we checked the radar images and found differences in the prevalent precipitating systems between the two regions. A considerable part of the ERCFs in region A were from well-organized systems like squall lines propagating from the northwest to the southeast, which may be favored by the stronger low-level wind shears; however, these systems became less organized when propagating to region B. On the contrary, in region B, more ERCFs are from the precipitating systems propagating from the southwest to the northeast with much smaller coverages, and tended to form in environments with weak low-level wind shears. We surmise that the larger areas of the ERCFs in region A can protect the updraft cores from the potential suppression effect of entrainment.

The underlying surface could also play an important role in extreme rainfall occurrence. First, the highr terrains in region A (Fig. 7f) may facilitate the convection development and updrafts (Chu and Lin, 2000). As a result, the stronger updrafts in region A can prompt the riming process and lightning and lead to the differences in the microphysical characteristics and processes between the two regions (Carey and Rutledge, 2000; Gauthier et al., 2006). On the other hand, most of the underlying surface of region B (A) is urban (rural), which could be a factor leading to the differences in conditions of thermodynamics and aerosol concentrations in the two regions. The impact of the urban surface will be further discussed in the next section.

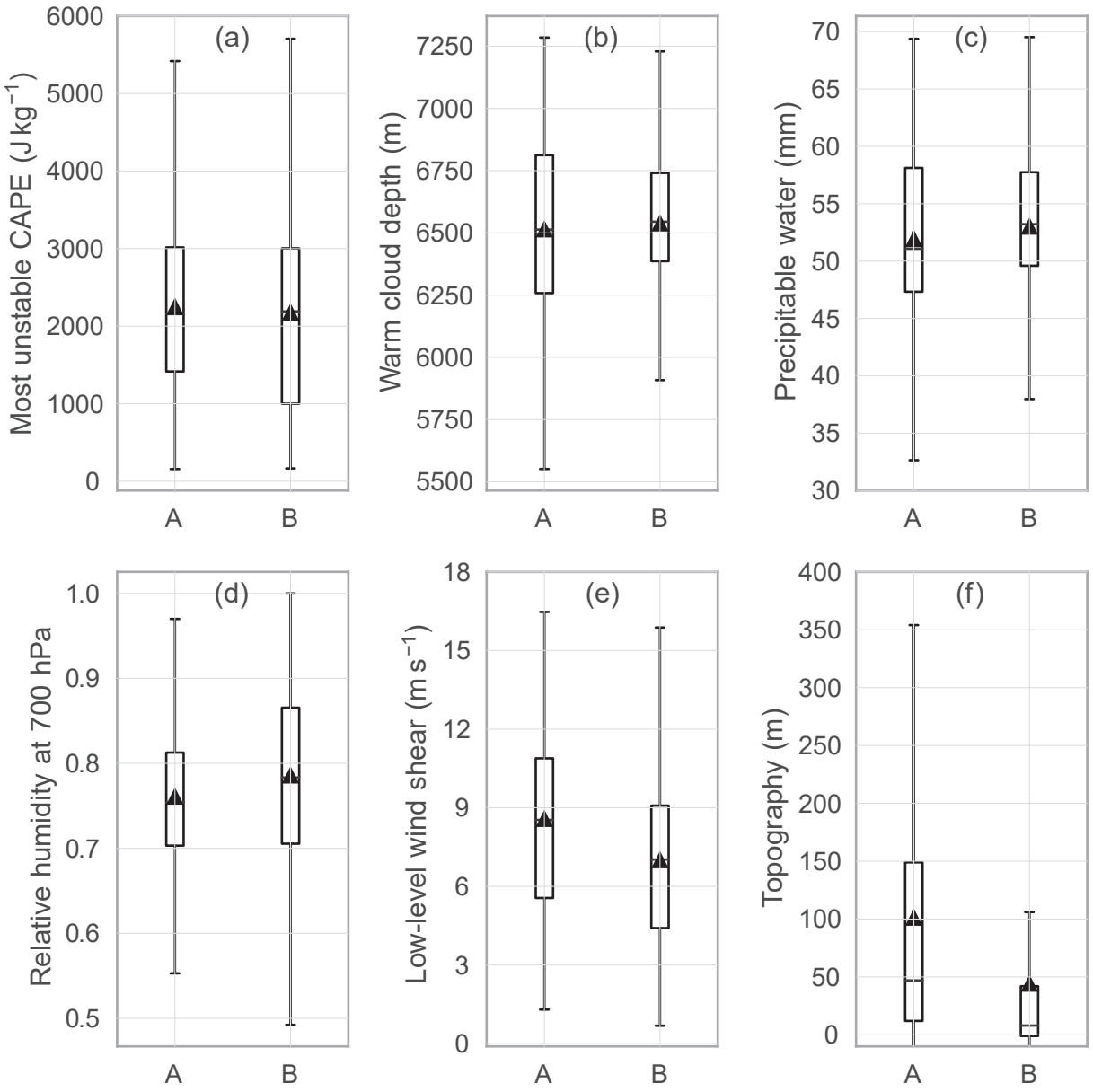

Fig. 7. Same as Fig. 3 but for (a) the most unstable convective available potential energy (MUCAPE), (b) warm cloud depth (WCD), (c) precipitable water (PW) in the warm cloud layer, (d) relative humidity at 700 hP, and (e) magnitude of low-level wind shear between the lifted condensation level (LCL) and 700-hPa level corresponding to the ERCFs whose reflectivity factor-normalized center is located in region A or region B (*x*-axis). These indices in (a–e) are calculated from the profiles extracted from the ERA5 reanalysis dataset. Panel (f) shows the distributions of terrain heights for the radar grids in regions A and B.

For further illustration of low-level conditions corresponding to the regional differences, the composites fields of 925-hPa relative humidity, wind, divergence, and surface wind at the times of occurrence of the ERCFs located in regions A and B are shown in Fig. 8. For the ERCFs in both regions, the composite onshore southeast winds blow from the SCS to the land at 925 hPa, carrying plenty of moisture to regions A and B. Upon detailed examination, it was found that the composite wind speeds at 925 hPa and the surface are higher for the ERCFs in region A than those for region B. In Figs. 8a and c, decelerations of the winds mainly occur in region A and the regions to its northeast, leading to the significant convergence there. Meanwhile, the higher terrains in region A, together with the higher low-level southerly wind, cause a stronger mechanical lifting effect compared to region B. Within this nearly saturated background (> 90%), the stronger divergence and lifting effect of topography in region A jointly promoted the development of extreme convention there.

By comparison, for the ERCFs in region B, the deceleration of the composite winds (Figs. 8b, d) mainly begins near the shorelines, with a local maximum convergence located

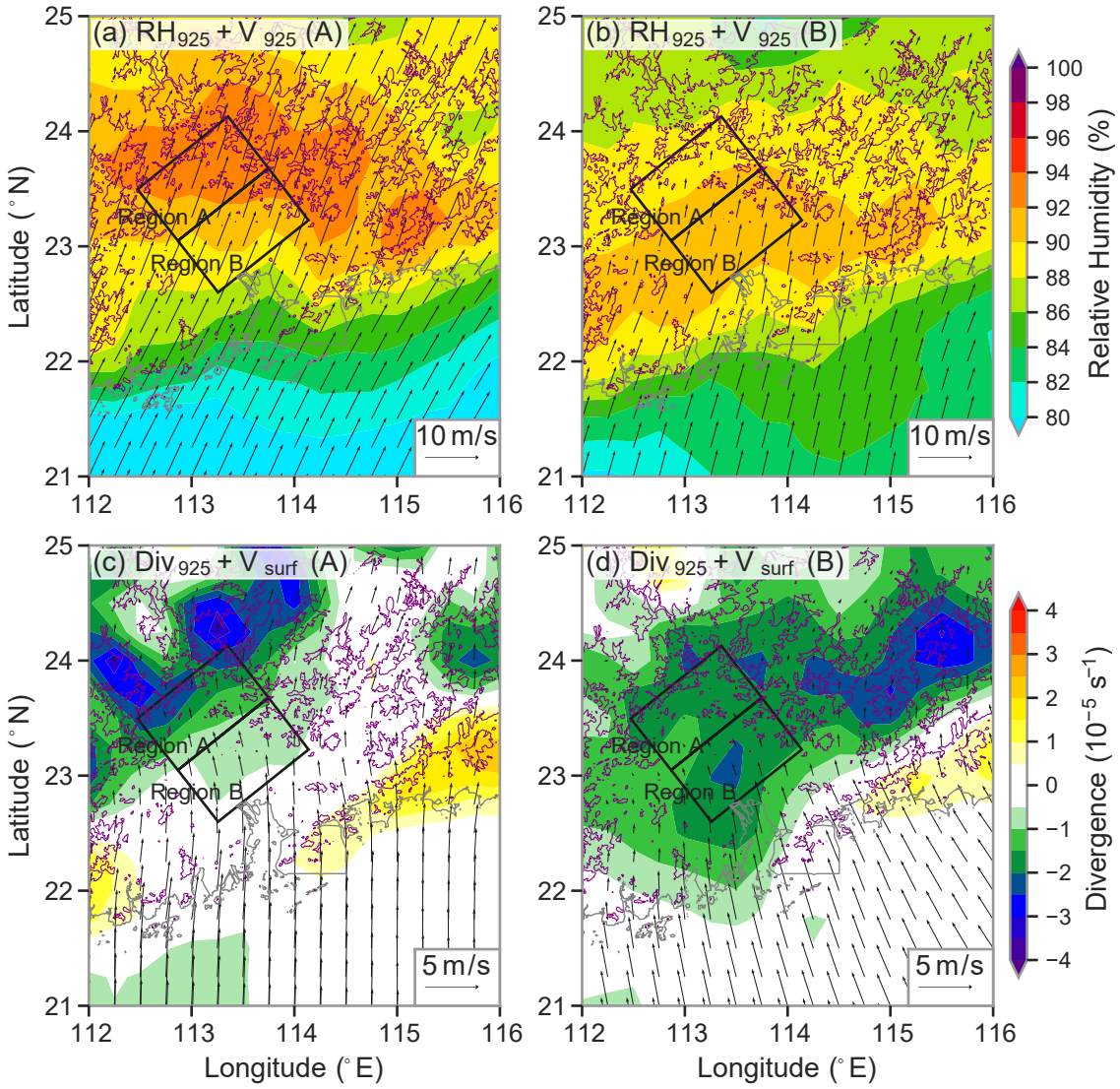

Fig. 8. Composite analysis of 925-hPa relative humidity [shading in (a) and (b)], 925-hPa wind [vectors in (a) and (b)], 925-hPa divergence [shading in (c) and (d)], and surface wind [vectors in (c) and (d)] from the ERA5 dataset at the times of occurrence of the ERCFs located in region A [(a) and (c)] and region B [(b) and (d)]. Two rectangles represent the regions of interest: Region A and Region B. The grey curves represent coastlines. The purple contours represent the 250-m topography.

within region B, which may be the main reason for the convection development there. When the ERCFs occur in region B, the wind speeds in region A are relatively weak and the relative humidity is < 90%, which is less favorable for convection development. From the composite synoptic conditions, one may find that the stronger low-level convergence, winds, and the topography dynamically favor the convection organization of the ERCFs in region A (Figs. 8a, c). For the ERCFs in region B, the dynamical conditions (low-level convergence) are relatively weak, which may lead to less convective organization, weaker updrafts, and weaker ice processes there.

4. Discussion and Conclusions

In this study, more than 2600 CFs with extreme rainfall rates are identified by grouping the contiguous convective regions from S-band polarimetric radar observations over a typical monsoon region (the Pearl River Delta, South China) in May and June from 2016 to 2018, defined as the ERCFs. The corresponding microphysical characteristics and processes are investigated, with an emphasis on the sub-regional differences in CFs exhibiting different lightning flash rates. Generally, the ERCFs with higher LFRs have higher mean echo tops, larger spanning areas, and larger volumes of high reflectivity above the freezing level, suggesting stronger updraft and more active ice microphysical processes within these precipitating systems.

Regional differences are also found for the vertical microphysical structures of the ERCFs. Above the freezing layer, the mean Z_H (Z_{DR}) of the ERCFs is generally higher (lower) in the regions with high LFRs, probably indicative of the exis-

tence of larger or more graupel particles; while in the regions with low LFRs, the lower Z_H and larger Z_{DR} indicate the potential presence of ice crystals and aggregates. Below the freezing layer, the ERCFs in the region with high LFRs generally have a larger mean raindrop size compared to the region with low LFRs. Furthermore, raindrop collision and coalescence contributes to the raindrop size growth of the ERCFs in both regions. Above the 4-km altitude in both regions, the warm-rain growth (converting cloud drops to raindrops) and the melting process makes an important contribution to the rapid increase of the LWC with decreasing altitude (larger in the region with high LFRs). However, below the 4-km altitude, the warm-rain process is more dominant for the ERCFs in the region with lower LFRs than in the other region.

The analyses of the weather condition show that in the region with relatively lower LFRs, the ERCFs are characterized by weaker low-level wind shear and more water vapor below the melting layer, leading to the rapid LWC increases by the dominant warm-rain growth processes, compared to those in the region with higher LFRs. It is also found that the mean MUCAPE values do not show a clear difference for the ERCFs between these two regions. This demonstrates that the difference in the microphysical characteristics and structures of the ERCFs in the two sub-regions is not caused by the difference in the unstable energy but due to other reasons, which is different from that found in previous studies (e.g., Hamada et al., 2015). Instead, the ERCFs in region A occur under the environment with strong low-level convergence and a relatively larger low-level wind shear, which leads to a higher degree of convective organization. With similar MUCAPE values (> 2000 J kg^{-1}), the larger areas of the more organized ERCFs in region A may mitigate the potential suppression effect of entrainment and produce stronger updrafts together with the greater topographic forcing, which prompts the riming process and lightning discharge processes.

For the ERCFs in region B, the impact of the urban-type surface should be mentioned. First, the urban areas could be an enhanced source of moisture (Dixon and Mote, 2003), and may lead to wind deceleration and convergence (Coceal and Belcher, 2004). The urban heat island effect could also be important for the development of the specific weather conditions facilitating the warm-rain processes, e.g., a well-mixed warm and humid boundary layer (Sun et al., 2021), but this conjecture is beyond the scope of the current study.

Using the observations from the polarimetric radar, we have studied two different microphysical mechanisms for the extreme rainfall in south China, but it is also important to address some potential limitations to this study. First, we have used the observations from only one polarimetric radar (i. e., Guangzhou S-POL) here. Due to the limitation of sampling, the accuracy of the observed and retrieved variables can vary with different distances from the radar site. A three-dimensional radar mosaic would be helpful for such a study in the future, but this also requires careful cross-radar calibration and quality control processes, especially for the polarimetric variables. Secondly, most of the retrieval algorithms based on polarimetric variables have been adapted using local DSD observations (e.g., Huang et al., 2020) except the one for IWC. The complexity of the ice habits and the lack of observations cause uncertainty in the IWC retrieval. With more aircraft-based hydrometeor observations in China in the future, the retrieval of IWC (as well as particle size distribution) will be improved, which can give more useful information for ice microphysics studies.

Acknowledgements. The authors would like to thank the scientists and engineers working on Guangzhou S-POL, the south-China ENTLS, the ERA5 reanalysis, and the DMSP/OLS nighttime light dataset. The DMSP/OLS nighttime light dataset can be downloaded at https://www.ngdc.noaa.gov/eog/dmsp/downloadV4composites.html. The extreme-rainfall convective feature dataset used in this work is available at https://doi.org/10.5281/zenodo.6331267. This work is primarily supported by the National Natural Science Foundation of China (Grant Nos. 42025501, 41905019, and 61827901) and the National Key Research and Development Program of China (Grant 2018YFC1506404 and Grant 2017YFC1501703) . The authors also thank Dr. Haonan CHEN (CSU) and Prof. Anning HUANG (NJU) for their suggestions on this work.

REFERENCES

Brauer, N. S., J. B. Basara, C. R. Homeyer, G. M. McFarquhar, and P. E. Kirstetter, 2020: Quantifying precipitation efficiency and drivers of excessive precipitation in post-landfall hurricane harvey. *Journal of Hydrometeorology*, **21**, 433–452, https://doi.org/10.1175/JHM-D-19-0192.1.

Bringi, V. N., V. Chandrasekar, J. Hubbert, E. Gorgucci, W. L. Randeu, and M. Schoenhuber, 2003: Raindrop size distribution in different climatic regimes from disdrometer and dual-polarized radar analysis. *J. Atmos. Sci.*, **60**, 354–365, https://doi.org/10.1175/1520-0469(2003)060<0354:RSDIDC>2.0.CO;2.

Bringi, V. N., M. A. Rico-Ramirez, and M. Thurai, 2011: Rainfall estimation with an operational polarimetric C-band radar in the United Kingdom: Comparison with a gauge network and error analysis. *Journal of Hydrometeorology*, **12**, 935–954, https://doi.org/10.1175/JHM-D-10-05013.1.

Carey, L. D., and S. A. Rutledge, 2000: The relationship between precipitation and lightning in tropical island convection: A C-band polarimetric radar study. *Mon. Wea. Rev.*, **128**, 2687–2710, https://doi.org/10.1175/1520-0493(2000)128<2687:TRBPAL>2.0.CO;2.

Chen, F. J., Y. F. Fu, and Y. J. Yang, 2019a: Regional variability of precipitation in tropical cyclones over the western north pacific revealed by the GPM dual-frequency precipitation radar and microwave imager. *J. Geophys. Res.*, **124**, 11 281–11 296, https://doi.org/10.1029/2019JD031075.

Chen, G., and Coauthors, 2019b: Microphysical characteristics of three convective events with intense rainfall observed by polarimetric radar and disdrometer in Eastern China. *Remote Sensing*, **11**, 2004, https://doi.org/10.3390/rs11172004.

Chen, H. N., V. Chandrasekar, and R. Bechini, 2017: An improved dual-polarization radar rainfall algorithm (DROPS2.0): Application in NASA IFloodS field campaign. *Journal of Hydrometeorology*, **18**, 917–937, https://doi.org/10.1175/JHM-D-16-0124.1.

Chen, Q., J. W. Fan, S. Hagos, W. I. Gustafson Jr., and L. K. Berg, 2015: Roles of wind shear at different vertical levels: Cloud system organization and properties. *J. Geophys. Res.*, **120**, 6551–6574, https://doi.org/10.1002/2015JD023253.

Chu, C.-M., and Y.-L. Lin, 2000: Effects of orography on the generation and propagation of mesoscale convective systems in a two-dimensional conditionally unstable flow. *J. Atmos. Sci.*, **57**, 3817–3837, https://doi.org/10.1175/1520-0469(2001)057<3817:EOOOTG>2.0.CO;2.

Cifelli, R., W. A. Petersen, L. D. Carey, S. A. Rutledge, and M. A. F. da Silva Dias, 2002: Radar observations of the kinematic, microphysical, and precipitation characteristics of two MCSs in TRMM LBA. *J. Geophys. Res.*, **107**, 8077, https://doi.org/10.1029/2000JD000264.

Coceal, O., and S. E. Belcher, 2004: A canopy model of mean winds through urban areas. *Quart. J. Roy. Meteor. Soc.*, **130**, 1349–1372, https://doi.org/10.1256/qj.03.40.

Deierling, W., W. A. Petersen, J. Latham, S. Ellis, and H. J. Christian, 2008: The relationship between lightning activity and ice fluxes in thunderstorms. *J. Geophys. Res.*, **113**, D15210, https://doi.org/10.1029/2007JD009700.

Ding, Y. H., C. Y. Li, and Y. J. Liu, 2004: Overview of the South China sea monsoon experiment. *Adv. Atmos. Sci.*, **21**, 343–360, https://doi.org/10.1007/BF02915563.

Dixon, M., 2015. Radx C++ software package for radial radar data, [Available from https://github.com/NCAR/lrose-core/tree/master/codebase/apps/Radx/src/Radx2Grid]

Dixon, P. G., and T. L. Mote, 2003: Patterns and causes of Atlanta's urban heat island–initiated precipitation. *J. Appl. Meteorol. Climatol.*, **42**, 1273–1284, https://doi.org/10.1175/1520-0450(2003)042<1273:PACOAU>2.0.CO;2.

Dolan, B., S. A. Rutledge, S. Lim, V. Chandrasekar, and M. Thurai, 2013: A robust C-band hydrometeor identification algorithm and application to a long-term polarimetric radar dataset. *J. Appl. Meteorol. Climatol.*, **52**, 2162–2186, https://doi.org/10.1175/JAMC-D-12-0275.1.

Dolan, B., B. Fuchs, S. A. Rutledge, E. A. Barnes, and E. J. Thompson, 2018: Primary modes of global drop size distributions. *J. Atmos. Sci.*, **75**, 1453–1476, https://doi.org/10.1175/JAS-D-17-0242.1.

Doswell III, C. A., 1985: The operational meteorology of convective weather. Volume II. Storm scale analysis. NOAA technical memorandum ERL ESG 15, 240 pp.

Gauthier, M. L., W. A. Petersen, L. D. Carey, and H. J. Christian Jr., 2006: Relationship between cloud-to-ground lightning and precipitation ice mass: A radar study over Houston. *Geophys. Res. Lett.*, **33**, L20803, https://doi.org/10.1029/2006GL027244.

Goodman, S. J., D. E. Buechler, P. D. Wright, and W. D. Rust, 1988: Lightning and precipitation history of a microburst-producing storm. *Geophys. Res. Lett.*, **15**, 1185–1188, https://doi.org/10.1029/GL015i011p01185.

Hamada, A., Y. N. Takayabu, C. T. Liu, and E. J. Zipser, 2015: Weak linkage between the heaviest rainfall and tallest storms. *Nature Communications*, **6**, 6213, https://doi.org/10.1038/ncomms7213.

Hersbach, H., and Coauthors, 2020: The ERA5 global reanalysis. *Quart. J. Roy. Meteor. Soc.*, **146**, 1999–2049, https://doi.org/10.1002/qj.3803.

Huang, H., and Coauthors, 2018: Quantitative precipitation estimation with operational polarimetric radar measurements in Southern China: A differential phase–based variational approach. *J. Atmos. Oceanic Technol.*, **35**, 1253–1271, https://doi.org/10.1175/JTECH-D-17-0142.1.

Huang, H., K. Zhao, G. F. Zhang, D. M. Hu, and Z. W. Yang, 2020: Optimized raindrop size distribution retrieval and quantitative rainfall estimation from polarimetric radar. *J. Hydrol.*, **580**, 124248, https://doi.org/10.1016/j.jhydrol.2019.124248.

Istok, M. J., and Coauthors, 2009: WSR-88D dual polarization initial operational capabilities. Preprints, *25th Conf. on International Interactive Information and Processing Systems (IIPS) for Meteorology, Oceanography, and Hydrology*, Phoenix, AZ, Amer. Meteor. Soc.

Kumjian, M. R., and A. V. Ryzhkov, 2010: The impact of evaporation on polarimetric characteristics of rain: Theoretical model and practical implications. *J. Appl. Meteorol. Climatol.*, **49**, 1247–1267, https://doi.org/10.1175/2010JAMC2243.1.

Kumjian, M. R., and O. P. Prat, 2014: The impact of raindrop collisional processes on the polarimetric radar variables. *J. Atmos. Sci.*, **71**, 3052–3067, https://doi.org/10.1175/JAS-D-13-0357.1.

Li, F. Y., D. Rosa, W. D. Collins, and M. F. Wehner, 2012: "Super-parameterization": A better way to simulate regional extreme precipitation. *Journal of Advances in Modeling Earth Systems*, **4**, M04002, https://doi.org/10.1029/2011MS000106.

Liu, C. T., and E. J. Zipser, 2009: "Warm Rain" in the tropics: Seasonal and regional distributions based on 9 yr of TRMM data. *J. Climate*, **22**, 767–779, https://doi.org/10.1175/2008JCLI2641.1.

Liu, C. T., and E. Zipser, 2013a: Regional variation of morphology of organized convection in the tropics and subtropics. *J. Geophys. Res.*, **118**, 453–466, https://doi.org/10.1029/2012JD018409.

Liu, C. T., and E. J. Zipser, 2013b: Why does radar reflectivity tend to increase downward toward the ocean surface, but decrease downward toward the land surface. *J. Geophys. Res.*, **118**, 135–148, https://doi.org/10.1029/2012JD018134.

Liu, C. T., D. J. Cecil, E. J. Zipser, K. Kronfeld, and R. Robertson, 2012: Relationships between lightning flash rates and radar reflectivity vertical structures in thunderstorms over the tropics and subtropics. *J. Geophys. Res.*, **117**, D06212, https://doi.org/10.1029/2011JD017123.

May, R., and Z. Bruick, 2019: MetPy: An community-driven, open-source python toolkit for meteorology. Preprints, *American Geophysical Union Fall Meeting 2019*, NS21A-16.

McKnight, P. E., and J. Najab, 2010: Mann-whitney U test. *The Corsini Encyclopedia of Psychology*, 4th ed., I. B. Weiner and W. E. Craighead, Eds., John Wiley & Sons, Inc., https://doi.org/10.1002/9780470479216.corpsy0524.

Naccarato, K. P., M. M. F. Saba, C. Schumann, O. Pinto, C. Medeiros, and S. Heckman, 2013: Waveform analysis of cloud-to-ground flashes as detected by fast e-field antennas and lightning location systems: On the way to precisely estimate the stroke peak current. Preprints, *2013 International Symposium on Lightning Protection*, Belo Horizonte, IEEE, 57–61, https://doi.org/10.1109/SIPDA.2013.6729196.

Nielsen, E. R., and R. S. Schumacher, 2020: Dynamical mechanisms supporting extreme rainfall accumulations in the houston "Tax Day" 2016 Flood. *Mon. Wea. Rev.*, **148**, 83–109, https://doi.org/10.1175/MWR-D-19-0206.1.

Petersen, W. A., and S. A. Rutledge, 1998: On the relationship between cloud-to-ground lightning and convective rainfall. *J. Geophys. Res.*, **103**, 14 025–14 040, https://doi.org/10.1029/97JD02064.

Piao, S. L., and Coauthors, 2010: The impacts of climate change on water resources and agriculture in China. *Nature*, **467**, 43–51, https://doi.org/10.1038/nature09364.

Saunders, C. P. R., 1993: A review of thunderstorm electrification processes. *J. Appl. Meteorol. Climatol.*, **32**, 642–655, https://doi.org/10.1175/1520-0450(1993)032<0642:AROTEP>2.0.CO;2.

Steiner, M., R. A. Houze Jr., and S. E. Yuter, 1995: Climatological characterization of three-dimensional storm structure from operational radar and rain gauge data. *J. Appl. Meteorol. Climatol.*, **34**, 1978–2007, https://doi.org/10.1175/1520-0450(1995)034<1978:CCOTDS>2.0.CO;2.

Sun, J. Z., 2005: Initialization and numerical forecasting of a supercell storm observed during STEPS. *Mon. Wea. Rev.*, **133**, 793–813, https://doi.org/10.1175/MWR2887.1.

Sun, X. Y., and Coauthors, 2021: On the localized extreme rainfall over the great bay area in South China with complex topography and strong UHI effects. *Mon. Wea. Rev.*, **149**, 2777–2801, https://doi.org/10.1175/MWR-D-21-0004.1.

Takahashi, T., T. Kawano, and M. Ishihara, 2015: Different precipitation mechanisms produce heavy rain with and without lightning in Japan. *J. Meteor. Soc. Japan*, **93**, 245–263, https://doi.org/10.2151/jmsj.2015-014.

Vincent, B. R., L. D. Carey, D. Schneider, K. Keeter, and R. Gonski, 2003: Using WSR-88D reflectivity data for the prediction of cloud-to-ground lightning: A central North Carolina study. *Natl. Wea. Dig*, **27**, 35–44.

Vitale, J. D., and T. Ryan, 2013: Operational recognition of high precipitation efficiency and low-echo-centroid convection. *Journal of Operational Meteorology*, **1**, 128–143, https://doi.org/10.15191/nwajom.2013.0112.

Wang, M. J., K. Zhao, W.-C. Lee, and F. Q. Zhang, 2018: Microphysical and kinematic structure of convective-scale elements in the inner rainband of typhoon matmo (2014) after landfall. *J. Geophys. Res.*, **123**, 6549–6564, https://doi.org/10.1029/2018JD028578.

Wu, P., B. K. Xi, X. Q. Dong, and Z. B. Zhang, 2018: Evaluation of autoconversion and accretion enhancement factors in general circulation model warm-rain parameterizations using ground-based measurements over the Azores. *Atmospheric Chemistry and Physics*, **18**, 17 405–17 420, https://doi.org/10.5194/acp-18-17405-2018.

Xu, W. X., and E. J. Zipser, 2012: Properties of deep convection in tropical continental, monsoon, and oceanic rainfall regimes. *Geophys. Res. Lett.*, **39**, L07802, https://doi.org/10.1029/2012GL051242.

Xu, W. X., E. J. Zipser, and C. T. Liu, 2009: Rainfall characteristics and convective properties of Mei-Yu precipitation systems over South China, Taiwan, and the South China Sea. *Part I: TRMM observations. Mon. Wea. Rev.*, **137**, 4261–4275, https://doi.org/10.1175/2009MWR2982.1.

Zhang, G., J. Vivekanandan, and E. Brandes, 2001: A method for estimating rain rate and drop size distribution from polarimetric radar measurements. *IEEE Trans. Geosci. Remote Sens.*, **39**, 830–841, https://doi.org/10.1109/36.917906.